Non-linear simulations of the TCV Scrape-Off Layer

F. Nespoli[1], I. Furno[1], F.D. Halpern[1], B. Labit[1], J. Loizu[2,3], P. Ricci[1], F. Riva[1]
[1] *École Polytechnique Fédérale de Lausanne (EPFL), Swiss Plasma Center (SPC), CH-1015 Lausanne, Switzerland*
[2] *Max Planck-Institut fur Plasmaphysik, D-17491 Greifswald, Germany*
[3] *Princeton Plasma Physics Laboratory, P.O. Box 451, Princeton, New Jersey 08543, USA*

Abstract

To investigate the mechanisms leading to the heat deposition onto the first wall in the Scrape-Off Layer (SOL), we perform dedicated numerical non-linear simulations of the SOL plasma dynamics of a TCV discharge using the GBS code. The simulated parallel heat flux profiles on the limiter agree qualitatively with the experimental ones obtained by means of infrared thermography, showing a double scale length. Non-ambipolar currents are found to flow to the limiter, consistenlty with the experiments. The contribution of the latters to the total heat flux is discussed. The results of a second simulation identical to the first one but with 40 times higher resistivity are also discussed.

1 Introduction

Inboard limited L-mode discharges are foreseen in ITER for the start-up and ramp-down phases resulting in large heat fluxes deposited from the plasma onto the first wall [1]. To measure such heat fluxes, dedicated experiments were performed in many tokamaks [2, 3, 4] among which TCV [5]. In all cases, two distinct regions in the Scrape-Off Layer (SOL) were observed. The near SOL, extending a few millimeters from the last closed flux surface (LCFS), is characterized by a steep gradient of plasma density and temperature and determines the peak of the heat load on the first wall. Attempts have been made to describe the near SOL width with the heuristic drift model [6] or the suppression of turbulence given by the shear of poloidal velocity [7]. The far SOL, characterized by flatter profiles, is typically a few centimeters wide and is at the origin of the main heat loss channel onto the first wall. The empirical scaling of the far SOL width has been recently investigated in Ref.[8]. Following the experimental evidence of the existence of two regions in the SOL, the design of the ITER first wall panels was changed to sustain a larger heat flux due to the near SOL [9]. Nevertheless, the physical mechanism at the origin of the double scale length in the SOL is not yet fully understood.

2 Non-linear simulations with the GBS code

To better understand the mechanisms leading to the heat deposition onto the first wall, we perform dedicated numerical non-linear simulations of the SOL plasma dynamics using the Global Braginskii Solver (GBS) code [10]. By solving the drift-reduced Braginskii equations, GBS allows for the self-consistent description of equilibrium and fluctuating quantities in a fully three-dimensional geometry. Effects due to finite aspect ratio, ion temperature and magnetic shear are included in the simulations. The equations determining the plasma dynamics and the boundary conditions at the limiters are detailed in Ref. [11] and [12, 13], respectively. Neumann boundary conditions are used for all quantities at the inner and outer radial boundaries of the simulations, with the exception of the plasma potential (at the outer boundary) and the vorticity (at both boundaries), for which Dirichlet conditions are imposed. These simulations feature only open field lines and the LCFS is set by the radial position of the plasma density and temperature source that mimics the injection of plasma

from the core. The position and amplitude of the sources could hence affect quantitatively the results. To better address the physics at the LCFS and in the near SOL, simulations including both open and closed field line regions are ongoing, whose first results are presented in Ref. [14].

In this paper, the results of two simulations are discussed: in the first one (A), the SOL of a TCV discharge is modeled. This is a circular inboard-limited ohmic L-mode deuterium plasma, with plasma current and toroidal magnetic field on axis being $I_p = 145$ kA and $B_\phi = 1.45$ T, respectively. The values of the plasma density and temperature at the LCFS, $n_{e,0} = 5 \times 10^{18}$ m^{-3} and $T_{e,0} = 25$ eV, are deduced from Langmuir probes embedded in the limiter. These parameters set the normalized Spitzer resistivity $\nu = q_e n_{e,0} R_0/(m_i c_{s,0} \sigma_\parallel) \propto n_{e,0} R_0 \Lambda m_e/(m_i c_{s,0} T_{e,0}^{3/2})$, $\nu = 5.9 \times 10^{-4}$, and the dimensionless size of the system through the ion sound Larmor radius $\rho_s = m_i c_{s,0}/(q_e B) = 0.5$ mm, where Λ is the Coulomb logarithm, R_0 is the major radius of the plasma, $c_{s,0} = \sqrt{k_b T_e/m_i}$ is the ion sound speed at the LCFS, and k_b is the Boltzmann constant. The resulting simulation domain consists of $128 \times 820 \times 128$ points in the radial (x), poloidal (y) and toroidal (z) direction, respectively. The sources of plasma temperature and density are located at $x = 20$. The shape of the sources is gaussian in the radial direction with a width of 3 grid points. The sources are poloidally and toroidally uniform. The safety factor $q = 3.2$, the magnetic shear $\hat{s} = 1.5$ and the inverse aspect ratio $\epsilon = 0.24$ are obtained from the magnetic reconstruction of the discharge. The ion temperature at the LCFS is assumed to be $T_{i,0} = T_{e,0}$. In this simulation, the toroidal magnetic field and the plasma current are antiparallel, while in the experiment they are parallel. This could lead to some discrepancies when comparing numerical and experimental results, since the direction of the drift velocities is reversed.

In Fig. 1, a snapshot of the plasma density from simulation A is shown, together with the limiter geometry for the simulation (thick red) and TCV (dashed red), respectively. The second simulation (B) is identical to the first one, exception made for the normalized resistivity which is 40 times larger. This choice is driven by the trend discussed in Ref. [5], i.e. that the heat flux associated with the near SOL increases with electron temperature and decreases with plasma density $\Delta P_{SOL} \propto T_e^{3/2} n_e^{-1} \propto \nu^{-1}$.

3 Comparison with the experimental data

The GBS numerical simulations provide the three-dimensional temporal evolution of the plasma density n (quasi-neutrality is assumed), the electron and ion temperature T_e and T_i, the electron and ion parallel velocities $v_{||,e}$, and $v_{||,i}$ and the plasma potential ϕ_p. The equilibrium 2D profiles are obtained averaging over time and over the toroidal direction. The plasma pressure and parallel current are computed as $p = n(T_e + T_i)$ and $j_{||} = en(v_{||,i} - v_{||,e})$ respectively. The parallel heat flux on the limiters is given by $q_{||} = q_{||,e} + q_{||,i}$, with $q_{||,e} = \frac{5}{2} n T_e v_{||,e} - 0.71 \frac{j_{||}}{e} T_e$ and $q_{||,i} = \frac{5}{2} n T_i v_{||,i} + \frac{1}{2} n v_{||,i}^3$.

The term including the kinetic energy of the net ion flow is often referred to as macroscopic heat flux. The term including the parallel current comes from the Braginskii closure of the energy equation and is referred to as microscopic heat flux. Finally, the terms proportional to ion and electron temperature are called mesoscopic heat fluxes, accounting for the thermal energy advected with the mean flow.

Fig. 2 shows the resulting heat flux profile for one of the two limiters and the comparison with the experimental profile. The simulated parallel heat flux radial profiles on the limiter are well described by a sum of two exponentials $q_{||} = q_s \exp(-r_u/\lambda_s) + q_l \exp(-r_u/\lambda_l)$, where r_u is the upstream coordinate (with $r_u = 0$ at the LCFS). The fitted values for simulation A, $\lambda_s = 2.3$ mm (2.5 mm) and $\lambda_l = 35$ mm (35 mm) for the upper (lower) limiter, respectively, are in quantitative agreement with the experimental ones obtained by means of infrared thermography $\lambda_{s,IR} = 3.2$ mm, $\lambda_{l,IR} = 37$ mm (the infrared analysis was possible only for the upper part of

the limiter). Nevertheless, the relative importance of the near SOL q_s/q_l is much smaller in the simulation than in the experiment: $(q_s/q_l)_{sim} = 0.4$ and $(q_s/q_l)_{exp} = 5$. If one neglects the near SOL and fits the whole profiles from the simulation with a single exponential, the resulting fall off lengths are $L_q = 57\rho_s$ ($50\rho_s$) for the upper (lower) limiter respectively. These values are in good agreement with the predictions of the adimensional scalings presentend in Ref. [15], both from quasi-linear theory ($L_{q,QL} = 43\rho_s$) and from the fit on the ITPA database published in Ref. [8] ($L_{q,fit} = 49\rho_s$).

A double scale length is observed in the pressure radial profiles as well. The pressure radial profiles fit well to a sum of two exponentials $p = p_s \exp(-r_u/\lambda_s) + p_l \exp(-r_u/\lambda_l)$. The poloidal variation of the two scale lengths is shown in Fig. 3, color coded with the relative strength of the near SOL p_s/p_l. In simulation A, two scale lengths are visible at all poloidal locations. The separation in scales is more pronounced in the bottom half of the the poloidal section. In simulation B, a net separation in scale lengths is present only in the proximity of the limiters, vanishing at the low field side.

Net electron currents flow to the limiter in the near SOL, as observed experimentally with Langmuir probes, suggesting their contribution to the formation of the narrow feature. Though, the simulated currents are one order of magnitude smaller than the measured ones, as it is shown in Fig. 4, where the simulation current poloidally averaged over 3 simulation points at the sheath entrance are compared with the experimental TCV data from the upper part of the limiter. The parallel current computed from the experimental data as $j_{||} = I_0/(A_p \sin\alpha)$, where I_0 is the current measured at ground potential and A_p is the geometric surface of the probe, is likely to be overestimated due to the vanishing angle α between the magnetic field and the probe surface, as one approaches the contact point ($r_u = 0$). The difference in behavior of such currents in the far SOL between the simulation and the experiment is under investigation and it is probably due to the Boussinesq approximation and the neglecting of the radial gradients in the boundary conditions. In Fig. 5, the microscopic heat flux associated with the non-ambipolar current is compared with the mesoscopic and microscopic ones. As a result, its contribution to the total heat flux is negligible. As suggested in Ref. [16], this confirms that although non-ambipolar currents are strictly related to the presence of a steep-gradient near SOL, they are not directly responsible for the excess heat flux to the limiter.

In simulation B, the heat flux profiles at the limiters are still well fitted by a sum of two exponentials. The increase of the resistivity causes the SOL to flatten and the poloidal asymmetry to increase. We find $\lambda_s = 8.3$ mm (5.0 mm), $\lambda_l = 164$ mm (62 mm) for the upper (lower) limiter, respectively. The widening of the far SOL and the increase of the poloidal asymmetry is observed in the pressure profiles as well, as shown in Fig.3 . The separation between the two scale lengths is sensible close to the limiters ($p_s/p_l \sim 0.5$), while it vanishes at the low field side ($p_s/p_l \sim 0.1$). The increase of resistivity also results in an overall reduction of the $\mathbf{E} \times \mathbf{B}$ velocity flow, as shown in Fig. 6, where the poloidal average of $v_{E\times B,\theta}$ is displayed for the two cases. In both simulations, the $\mathbf{E} \times \mathbf{B}$ flow is mainly poloidal towards the upper limiter, its radial component being negligible. As the resistivity is increased, the current flowing to the upper limiter is reduced by a factor 2, while the one flowing to the lower limiter does not vary substantially.

The poloidally averaged skewness profiles for density fluctuations are shown in Fig. 7 for both simulations. The skewness increases moving away from the LCFS, being > 0.5 in the far SOL. Also, as the resistivity is increased, the skewness increases by more than 30%. The positive skewness is an indication of the presence of blobs, which can play an important role in the transport in the far SOL. The dynamics of the blobs and their impact on heat transport in the SOL will be discussed in a future work [17].

4 Conclusions

First dedicated nonlinear numerical simulations of the TCV SOL are presented. The heat fluxes onto the limiter show the presence of two distinct regions in the SOL, similarly to the experimental data from IR thermography. The values of the near and far SOL decay lengths agree quantitatively with the experiments. Also, non-ambipolar electron currents flowing to the limiters are observed, qualitatively agreeing with the experiments. This confirms the correlation between non-ambipolar currents and the formation of a double scale length in the SOL. The heat flux associated with such currents does not contribute substantially to the total heat flux deposited onto the limiter.
Increasing the resistivity by a factor of 40 causes the drastic reduction of the poloidal $\mathbf{E} \times \mathbf{B}$ velocity, and the overall broadening of the SOL. The separation between the two scale lengths in the pressure profiles is more visible close to the limiters, not on the low field side. To shed light on the physics in the near SOL, a similar analysis will be applied to ongoing simulations which include both open and closed field line regions.

Acknowledgments

The simulations presented herein were carried out using the HELIOS supercomputer system at Computational Simulation Centre of International Fusion Energy Research Centre (IFERC-CSC), Aomori, Japan, under the Broader Approach collaboration between Euratom and Japan, implemented by Fusion for Energy and JAEA. This work has been carried out within the framework of the EUROfusion Consortium and has received funding from the Euratom research and training programme 2014-2018 under grant agreement No 633053. The views and opinions expressed herein do not necessarily reflect those of the European Commission.

References

[1] R.A. Pitts et al., J. Nucl. Mater. 415 (2011) 957-964

[2] G. Arnoux , et al., Nucl. Fusion 53 (2013)

[3] J. Horacek, et al., J. Nucl. Mater. 463 (2015)

[4] P.C. Stangeby, et al., J. Nucl. Mater. 463 (2015)

[5] F. Nespoli, et al., J. Nucl. Mater. 463 (2015) 393-396

[6] R.J. Goldston, J. Nucl. Mater. 463 (2015)

[7] F.D. Halpern and P. Ricci, submitted to Phys. of Plasmas (2016)

[8] J. Horacek, et al., Plasma Phys. Control. Fusion 58 (2016) 074005

[9] M. Kocan, et al., Nucl. Fusion 55 (2015) 033019

[10] P. Ricci et al., Plasma Phys. Controlled Fusion 54 (2012) 124047

[11] F. D. Halpern, et al., J. Comput. Phys. 315 (2016) 388-408

[12] J. Loizu, et al., Phys. of Plasmas 19 (2012) 122307

[13] A. Mosetto, et al., Phys. of Plasmas 22 (2015) 012308

[14] F. D. Halpern, 57th Annual Meeting of the APS DPP, Nov. 16-20, 2015, Savannah (GA)

[15] F. D. Halpern et al., Plasma Phys. Controlled Fusion 58 (2016) 084003

[16] R.Dejarnac et al., J. Nucl. Mater. 463 (2015) 381-384

[17] F. Nespoli, et al., to be submitted to Plasma Phys. Controlled Fusion (2016)

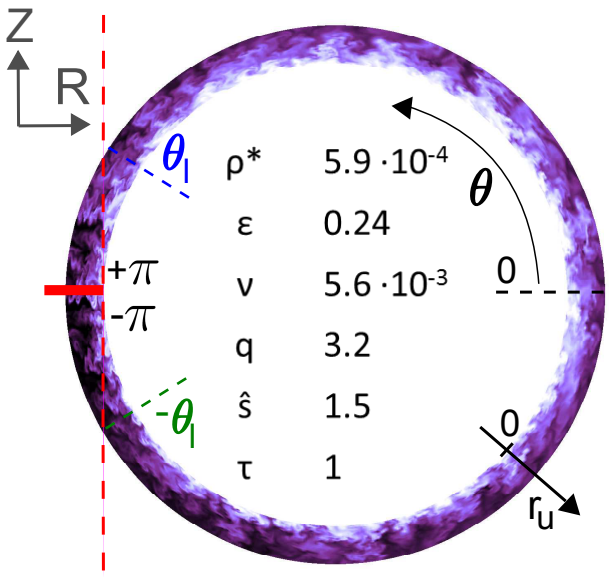

Figure 1: Snapshot of plasma density from simulation A. The coordinate system is displayed together with limiter geometry for the simulation (thick red) and TCV (dashed red). The simulation parameters are displayed: $\rho^* = \rho_s/R$, the inverse aspect ratio ϵ, the normalized Spitzer resistivity ν, the safety factor q, the magnetic shear $\hat{s}$ and $\tau = T_{i,0}/T_{e,0}$.

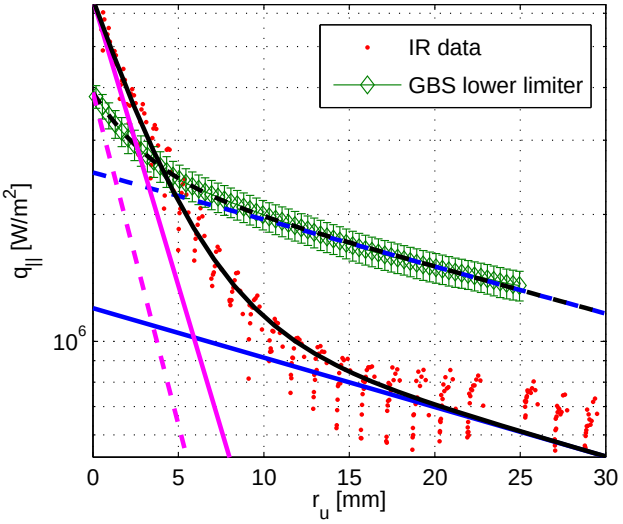

Figure 2: Heat flux onto the lower limiter (green diamonds) is compared with experimental data from IR thermography (red dots). The fit with the sum of two exponentials is shown (black lines), the short exponential in magenta and the long one in blue, continuous lines for experimental data and dashed lines for one of the two limiters in the simulation. The fitted lengths of far and near SOL are in good agreement between simulation and experiment, but not the magnitude of the associated heat fluxes.

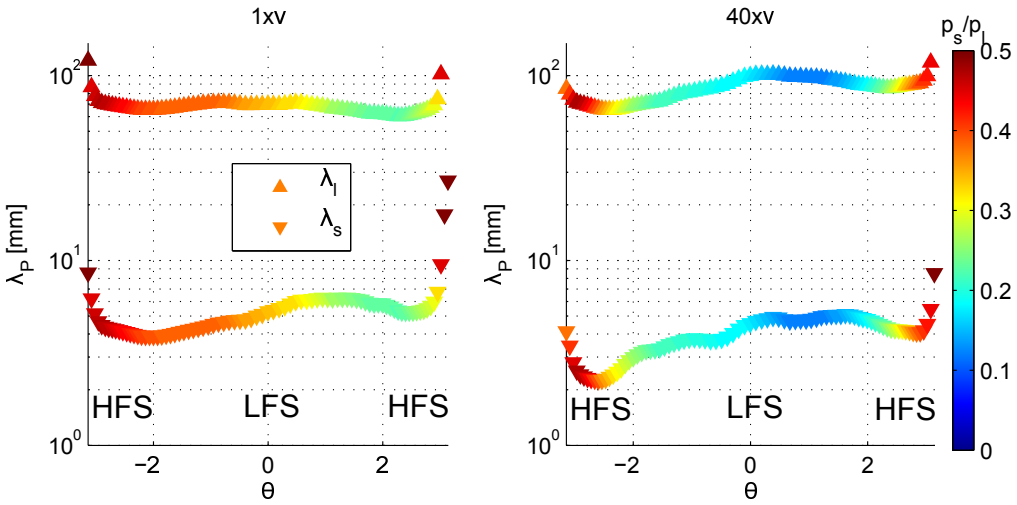

Figure 3: Poloidal variation of the two decay lengths resulting from the fit of the pressure profiles with the sum of two exponentials, color coded with the relative strength of the short component. Simulation A on the left, simulation B on the right. The increase of resistivity causes the near SOL to become relatively less important on the low field side.

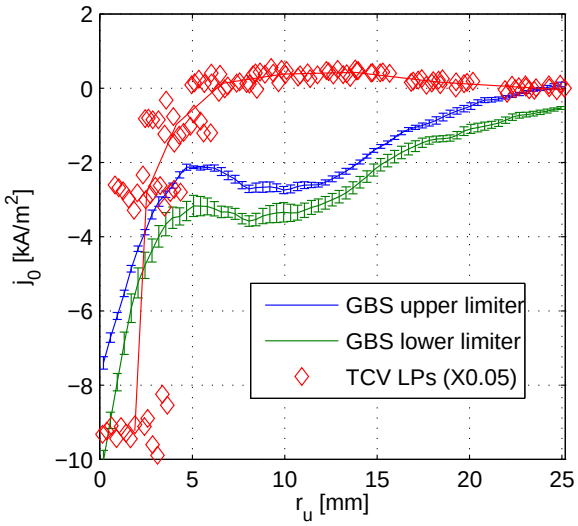

Figure 4: Parallel currents to the limiters in the GBS simulation A (blue and green). They qualitatively agree with the current density to the grounded wall measured in TCV with flush mounted Langmuir probes (red diamonds, rescaled for plotting).

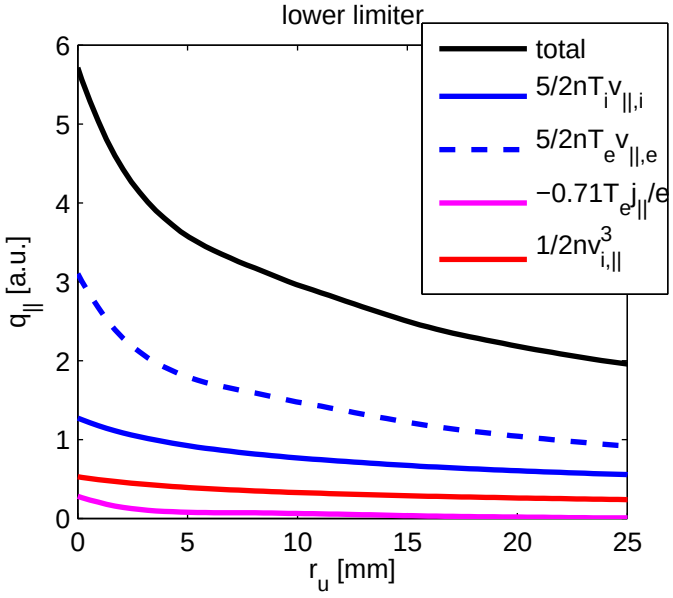

Figure 5: Different components contributing to the heat flux arriving onto the lower limiter in simulation A. The microscopic heat flux associated with the non-ambipolar currents (magenta line) contributes only marginally to the total heat flux. Similar results for the upper limiter.

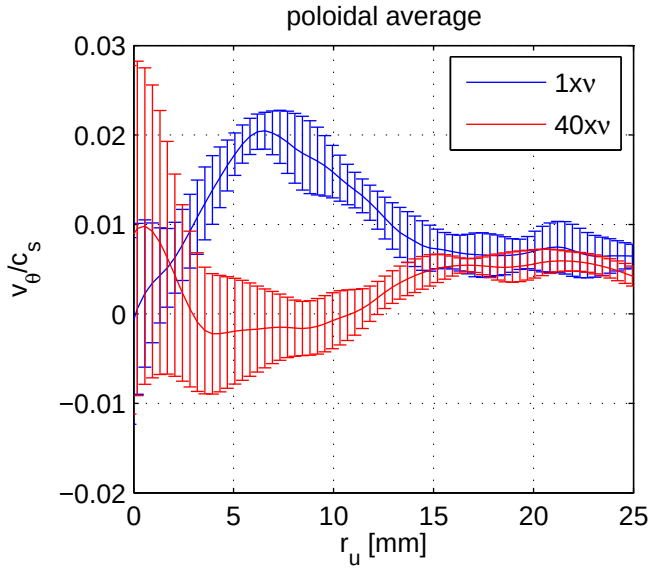

Figure 6: Poloidal average of the poloidal component of the $\mathbf{E} \times \mathbf{B}$ flow for simulation A (blue) and B (red). The error bars are given by the standard deviation over the poloidal profile. As the resistivity is increased, the poloidal flow is suppressed.

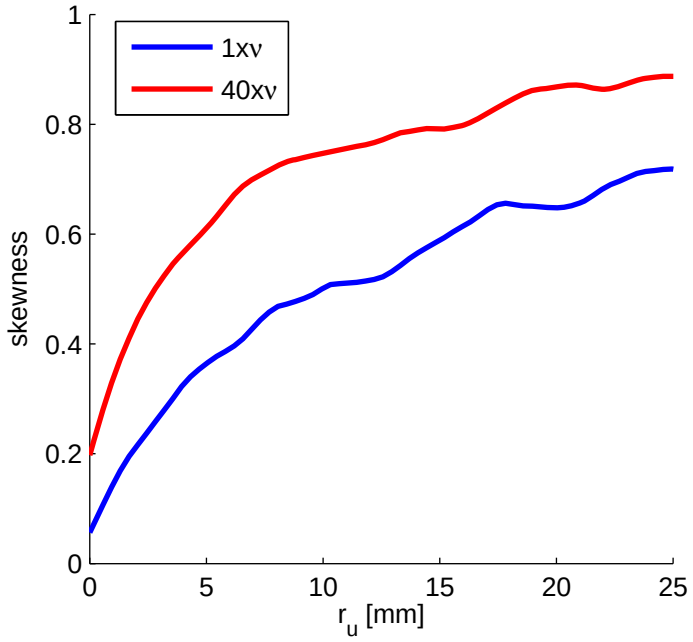

Figure 7: Poloidal average of the skewness of the density fluctuations for simulation A (blue) and B (red). The skewness increases moving away from the LCFS . The skewnees for simulation B is approximately 30% higher than in simulation A.